Occupancy of lattice positions probed by X-ray photoelectron diffraction : a case study of tetradymite topological insulators

Occupancy of lattice positions probed by X-ray photoelectron diffraction: A case study of tetradymite topological insulators

Nadezhda V. Vladimirova[1,2,3], Alexander S. Frolov[1,2,3], Jaime Sánchez-Barriga[4], Oliver J. Clark[4], Fumihiko Matsui[5], Dmitry Yu. Usachov[3,6], Matthias Muntwiler[7], Carolien Callaert[8], Joke Hadermann[8], Vera Neudachina[2], Marina E. Tamm[1], Lada V. Yashina[1,2]*

1) Lomonosov Moscow State University, Leninskie Gory 1/3, 119991 Moscow, Russia
2) N.N. Semenov Federal Research Center for Chemical Physics, Kosygina Street 4, 119991 Moscow, Russia
3) Center for Advanced Mesoscience and Nanotechnology, Moscow Institute of Physics and Technology, National Research University, 9 Institutskiy Pereulok, Dolgoprudny, Moscow Region 141700, Russia
4) Helmholtz-Zentrum Berlin für Materialien und Energie, Elektronenspeicherring BESSY II, Albert-Einstein-Str. 15, 12489 Berlin, Germany
5) Institute for Molecular Science, Okazaki 444-8585 Japan
6) St. Petersburg State University, 7/9 Universitetskaya nab., 199034 St. Petersburg, Russia
7) Laboratory for Micro- and Nanotechnology, Paul Scherrer Institute, 5232 Villigen PSI, Switzerland
8) EMAT, Department of Physics, University of Antwerp, Groenenborgerlaan 171, 2020 Antwerp, Belgium
*Corresponding author. E-mail: yashina@inorg.chem.msu.ru

Abstract

Occupancy of different structural positions in a crystal lattice often seems to play a key role in material properties. Several experimental techniques have been developed to uncover this issue, all of them being mostly bulk sensitive. However, many materials including topological insulators (TIs), which are among the most intriguing modern materials, are intended to be used in devices as thin films, for which the sublattice occupancy may differ from the bulk. One of the possible approaches to occupancy analysis is X-ray Photoelectron Diffraction (XPD), a structural method in surface science with chemical sensitivity. We applied this method in a case study of $Sb_2(Te_{1-x}Se_x)_3$ mixed crystals, which belong to prototypical TIs. We used high-angle annular dark field (HAADF) scanning transmission electron microscopy (STEM) as a reference method to verify our analysis. We revealed that the XPD data for vacuum cleaved bulk crystals are in excellent agreement with the reference ones. Also, we demonstrate that the anion occupancy near a naturally formed surface can be rather different from that of the bulk. The present results are relevant for a wide range of compositions where the system remains a topological phase, as we ultimately show by probing the transiently occupied topological surface state above the Fermi level by ultrafast photoemission.

Keywords

Occupancy, topological insulators, tetradymite, X-ray photoelectron diffraction, HAADF STEM

1. Introduction

Recently, various structural and physical aspects of topological insulators (TIs) have undergone thorough investigation due to their potential applications in novel electronic devices, for example, in spintronics and quantum computers [1–4]; such materials have a highly conductive surface combined with an insulating bulk. The electrons at the surface of TIs move in the opposite directions when having opposite spins, which opens the pathway for electronic and spin transport. Tetradymite-type compounds are among the most studied classes of TIs; in addition to the well-known binary compounds such as bismuth and antimony telluride, as well as bismuth selenide, solid solutions with a similar structure also display the properties of topological insulators. They are, in fact, even more attractive and promising for potential practical applications compared to the binary compounds, since all relevant parameters (e.g., the Fermi level energy, the bandgap, and the Dirac point position) can be varied in a relatively wide range depending on the composition. The bandgap increase can be more efficiently reached by anion substitution as

opposed to the cation substitution [5,6]. For TI solid solutions with anion substitution, a number of materials have been reported, namely, Bi_2Te_2Se, Sb_2Te_2Se, Bi_2Te_2S, Bi_2Te_2S, $Bi_{1.5}Sb_{0.5}Te_{1.7}Se_{1.3}$, $Bi_2Te_{1.6}S_{1.4}$, and $Bi_{1.1}Sb_{0.9}Te_2S$ [5–17]. Among them, the M_2Te_2Se phases (M=Bi, Sb) attract special attention as they possess certain intriguing and unique properties; for example, Sb_2Te_2Se displays large linear magnetoresistance combined with extremely low mobility [12,18,19], while its nanoflakes can be used to manufacture a high-performance visible light photodetector [14].

Occupancy of different structural positions by atoms of the same element in a crystal lattice of mixed crystals has been shown to influence certain material properties, for example, magnetic ordering (ferromagnetic or antiferromagnetic) [20,21] and quantum phase transitions [20,22] in TIs. Several experimental techniques have been developed and are currently used to characterize the occupancy and disordering, such as X-ray diffraction (XRD) with Rietveld refinement [8,23], single-crystal diffraction methods [24], [25], extended X-ray absorption fine structure (EXAFS) spectroscopy [25], and Mossbauer spectroscopy [26]; all of them are bulk-sensitive. However, many novel materials, including TIs, are intended to be used as thin films, in which the sublattice occupancy may differ from the bulk due to thermodynamically or kinetically induced surface segregation. Another issue with the most popular methods for occupancy analysis, for example, XRD with Rietveld refinement, is that it is impossible to simultaneously determine the site occupancy and the atomic displacement parameters (ADPs) correctly, which yields inaccurate occupancy values (in many cases the occupancy is fixed during Rietveld refinement based on the data obtained by other methods with higher locality, i.e., high-angle annular dark field (HAADF) scanning transmission electron microscopy (STEM) with electron energy loss spectroscopy (EELS) [27] or HAADF-STEM/energy dispersive X-ray (EDX) spectroscopy [28,29]).

Another possible approach to investigate the site occupancy for crystals or thin films is X-ray photoelectron diffraction (XPD), a structural method in surface science with chemical sensitivity [30], which makes it an ideal candidate for refined structural studies of thin films and surfaces. The XPD analysis with chemical state resolution is a well-established procedure, but not applicable here; in solid solutions, where atoms of the same elements occupy different lattice positions while having the same chemical shift, the structural analysis potentially can be done by applying the commonly known *R*-factor analysis while varying the corresponding occupancies; however, this idea so far has not been tested experimentally. Here, we perform a case study of solid solutions of tetradymite-type topological insulators with anion substitution by XPD and compare the results with well-established bulk sensitive methods to verify whether XPD can be applied to characterize the occupancy of various structural positions within a crystal lattice in a near-surface region.

Based on the arguments provided above, we decided to focus on testing the capability of XPD to help determine the occupancy in the $Sb_2(Te_{1-x}Se_x)_3$ tetradymite-type solid solutions. Anion substitution in such systems can lead either to statistically filled or ordered atomic positions; in tetradymite type crystals and thin films, usually, there is no cation ordering (as confirmed, for example, for Bi_2Te_3-Sb_2Te_3 [31]), while certain anion ordering has been often observed [11,32]. Within the quintuple layer of tetradymite-like structures, two different anion positions exist (as illustrated by Ch (1) and Ch (2) in Fig. 1a for $Sb_2(Te_{1-x}Se_x)_3$); the intralayer position is usually more energetically favorable for more electronegative anions [32,33]. The Sb_2Se_3-Sb_2Te_3 phase diagram [34] indicates that mixed crystals exist in the range of 0-64 mol.% Sb_2Se_3, where the solid solutions show nearly ideal behavior [35]. In $Sb_2(Te_{1-x}Se_x)_3$, based on the available data we can potentially expect Se atoms to occupy the intralayer positions up to $x = 0.33$ (which corresponds to Sb_2Te_2Se with Te-Sb-Se-Sb-Te quintuples). For Sb_2Te_2Se, early XPD and XRD/Rietveld studies are available, which in general indicate no disordering within the selenium intralayer [23,36]; however, the site occupancy was not quantitatively characterized in either of these works. Due to the developments within the past decades, new experimental capabilities should enable further clarification of this issue. It has been shown earlier that for similar bismuth solid solutions, specifically for the Bi_2Te_2Se crystals, which are of interest for thermoelectric applications, there is certain disordering in the selenium and tellurium layers (8.5% of Te in the intralayer and 4.3% of Se in the outer layers, respectively [8]), which agrees well with the available STM data (disordering corresponding to about 5% of Se in the outer Te layers [37]). These results indicate that modern experimental investigations of $Sb_2(Te_{1-x}Se_x)_3$, preferably in

a wider range of compositions not limited only to Sb_2Te_2Se, are required to characterize the anion disordering.

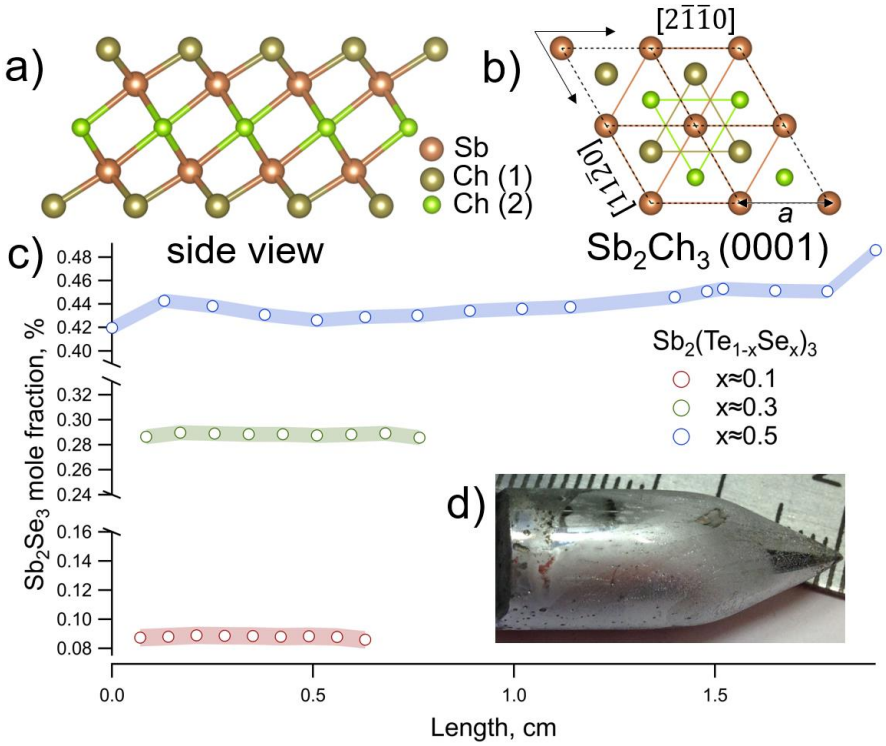

Fig. 1. (a) $Sb_2(Te_{1-x}Se_x)_3$ crystal structure with different possible chalcogen anion positions, Ch (1) and Ch (2); (b) Sb_2Se_3 fraction distribution along the $Sb_2(Te_{1-x}Se_x)_3$ crystal length according to the XRF data, line thickness corresponds to error bar ; (c) photo of a typical $Sb_2(Te_{1-x}Se_x)_3$ crystal, scale is in cm.

In this paper, we describe the occupancy determination from the XPD data for the $Sb_2(Te_{1-x}Se_x)_3$ solid solutions of three different compositions and compare the results with those obtained using other methods (HAADF-STEM/EDX, XRD with Rietveld refinement) as a new approach to determine the occupancy of various structural positions within the crystal lattice of thin films and 2D materials.

2. Methods

≈10 g $Sb_2(Te_{1-x}Se_x)_3$ crystals were grown from the melt by the Bridgman method using a procedure similar to that described in Ref. [38]. The compounds were synthesized directly in the growth ampoule. 1% Sb extra was added to all compositions as the homogeneity range of Sb_2Te_3 is shifted towards antimony [34]. The crystal growth took up to 7-9 days and was performed at a pulling rate of 0.75 cm/day. The temperature gradient during growth was set to be 10 K/cm. A typical view of the obtained crystal is shown in Fig. 1c. The obtained crystals were characterized by XRF and additionally by powder XRD. The XRF measurements were performed using a Bruker Mistral-M1 micro-focused system equipped with an XFlash 30mm^2 detector, the concentrations were determined using XSpect software by determining the area of individual peaks using the external standard model. 4-7 measurements were taken for each crystal. The average composition distribution along the crystal length as determined by XRF is illustrated in Fig. 1b. For XRD the samples were powdered and additionally annealed in evacuated sealed ampoules at 300^{0}C to eliminate mechanical stress. XRD was performed using a PANalytical Empyrean diffractometer equipped with a PSD Pixel3D detector in the 2θ range of 10-82^0 with a step of 0.02^0 at room temperature. The obtained data were treated within Jana 2006 software package using the PDF-2 database.

For HAADF–STEM imaging and EDX mapping, cross-sectional samples were prepared on a Cu support by focused ion beam (FIB) milling. The HAADF–STEM and EDX data were acquired on an aberration-corrected Thermo Fisher Scientific Titan transmission electron microscope operating at 200 kV

and equipped with a Super-X EDX detector. The HAADF-STEM simulations were performed using the MULTEM software package [39] and the QSTEM package [40].

The XPD data were acquired at room temperature at the PEARL (X03DA) beamline [42] of the Swiss Light Source using linearly polarized light. The (111) surfaces of the crystals were prepared by cleaving in vacuum along the van-der-Waals gap. The direction perpendicular to the sample surface, the light polarization, and the axis of the analyzer lens were oriented in the horizontal plane of the laboratory reference frame, while the entrance slit of the Scienta EW4000 electron analyzer was oriented vertically. For the acquisition of XPD maps Sb 4*d*, Te 4*d* and Se 3*d* photoemission peaks were measured at the same electron kinetic energy of 600 eV in order to provide the same probing depth for all the elements. XPD maps were acquired by rotating the sample with polar angle steps of 1°. The acceptance azimuthal angle of the analyzer was restricted to ±18°. The 2D electron detector allowed mapping of the angular distribution with azimuthal angle steps of less than 0.5°. The polar angle range was 80°, while the azimuthal angle range was 138°. For plotting XPD patterns we have used the equiareal Lambert azimuthal projection representation. Angular distribution of photocurrent was obtained by peak fitting of photoemission spectra $I(E)$ at each polar/azimuthal angle, then the data was symmetrized according to 3-fold crystal symmetry (I(phi)=I(phi+120^o)=I(phi+240^o)). Finally, XPD patterns are presented in this paper after removal of the background intensity, which is a smooth function of the polar angle. The calculation of XPD patterns was done with the electron diffraction in atomic clusters (EDAC) code [41]. The XPD patterns are presented in this paper after removal of the background intensity, which is a smooth function of the polar angle, in accordance with Ref. [42]. The R-factor calculation, its minimization procedure, and error estimation are described in [44]. This definition of the R-factor is slightly different from those proposed in Refs. [43,44] (it is not normalized to the background intensity). We used two parabolic clusters, Sb_2Te_3 and Sb_2Se_3, with the corresponding cell parameters, a radius of 40 Å, and two quintuple layers thickness. One cluster included about 3500 atoms. The emitting atom was located in the center of each layer in each cluster, and the occupancy was modeled as a fraction of Te and Se atoms in the same positions within the layer. Multiple photoelectron scattering was calculated by the iterative method to reach convergence. The maximal multiple scattering order (n) was set to 10. The calculations were performed at 300 K, temperature lattice vibrations were taken into account using a Debye-Waller factor for Sb, Se, and Te. The following parameters were optimized: Inner potential (V_0), Debye temperature ϑ_d, inelastic mean free path (IMFP), cell parameters for the cluster, occupancy of Ch (1) and Ch (2) positions (see Fig. 1a), etc. parabolic cluster radius R_{max} was chosen to be twice the IMFP. Full R-factor analysis was performed to evaluate the agreement between the experimental and theoretical data.

The pump-probe angle resolved photoemission spectroscopy (ARPES) experiments were carried out at the RGBL-2 station in Helmholtz-Zentrum Berlin using Ti: Sapphire fs oscillator coupled to an ultrafast amplifier laser system (RegA, Coherent) operated at 150 kHz. Photoelectrons were detected with a Scienta R4000 analyzer and the base pressure of the setup was ~1×10^{-10} mbar. The single crystals were cleaved in situ at room temperature. The 1.5 eV pump and 6 eV probe fs-laser pulses were incident on the sample under an angle of 45 degrees, and the time resolution was ~160 fs. The pump fluence was ~100 μJ/cm^2 and the angular and energy resolutions of the pump-probe ARPES measurements were 0.1◦ and 20 meV, respectively.

3. Results and Discussion

In the tetradymite structure shown in Fig. 1a, there are two different anion positions (1/3 of inner positions Ch (2) inside of the quintuple layer (QL) and 2/3 of outer positions Ch (1)), with the intralayer position being more energetically favorable for anions formed by more electronegative atoms [8]. For the purposes of this work, we consider a system to be fully ordered if all Se atoms are in the Ch(2) position (for $x \leq 1/3$), and if all Ch(2) positions are occupied only by Se atoms (for $x > 1/3$); a system is considered to be fully disordered if the probabilities of Se atoms to be in the Ch(1) and Ch(2) positions are equal.

To quantify this issues, we introduce here the ordering factor (α), where α=1 corresponds to a situation when upon an increase of Se content up to x=1/3 it occupies only the Ch(2) positions, then at x>1/3 it

starts to also fill in the Ch(1) positions (model **A**); α=0 corresponds to a structure where all Se atoms are in the Ch(1) positions up to *x*=2/3, then at *x*>2/3 Se atoms also fill in the Ch(2) positions (model **B**); α=0.5 corresponds to a fully disordered system. Since Se and Te atoms have similar electron scattering factors (see Supplementary materials, Section 1), and XPD is most sensitive to the local environment of the emitter, the resulting intensity of XPD pattern $I(\varphi,\Theta)$ can be calculated for each element as a linear combination of patterns corresponding to two limiting scenarios of ordering (A and B):

$$I_{(\varphi,\Theta)}^{Element} = \alpha * I_{(\varphi,\Theta)}^{A} + (1-\alpha) * I_{(\varphi,\Theta)}^{B}$$

In $Sb_2(Te_{1-x}Se_x)_3$, general structural and geometrical considerations show that for $x < \frac{1}{3}$

$$I_{(\varphi,\Theta)}^{Te} = \left(1 - \frac{3}{2}x(1-\alpha)\right) I_{(\varphi,\Theta)}^{Te(Ch1)} + (1-3x\alpha) I_{(\varphi,\Theta)}^{Te(Ch2)},$$

$$I_{(\varphi,\Theta)}^{Se} = \frac{3}{2}x(1-\alpha) I_{(\varphi,\Theta)}^{Se(Ch1)} + 3x\alpha I_{(\varphi,\Theta)}^{Se(Ch2)},$$

whereas for $\frac{1}{3} < x < \frac{2}{3}$

$$I_{(\varphi,\Theta)}^{Te} = \left(1 - \frac{1}{2}(3x-\alpha)\right) I_{(\varphi,\Theta)}^{Te(Ch1)} + (1-\alpha) I_{(\varphi,\Theta)}^{Te(Ch2)},$$

$$I_{(\varphi,\Theta)}^{Se} = \frac{1}{2}(3x-\alpha) I_{(\varphi,\Theta)}^{Se(Ch1)} + \alpha I_{(\varphi,\Theta)}^{Se(Ch2)},$$

where *x* is the mole fraction of Se in $Sb_2(Te_{1-x}Se_x)_3$, $I_{(\varphi,\Theta)}^{Ch(Ch1)}$ and $I_{(\varphi,\Theta)}^{Ch(Ch2)}$ are the XPD intensities obtained by uniting the patterns of the corresponding chalcogen emitters from the Ch (1) or Ch (2) layers, and α is the ordering factor introduced above. The ordering factor α was optimized in our calculations described below in order to achieve the minimum *R* values at the same time.

The occupancy and the corresponding ordering factor can vary with the solid solution composition. For this reason, we studied 3 different crystals of $Sb_2(Te_{1-x}Se_x)_3$: one with a low Se content corresponding to *x*≈0.1, the second one is of tetradymite stoichiometry, Sb_2Te_2Se, with x≈0.3, and the third crystal had a Se concentration close to the maximum, *x*≈0.5. The composition distribution along the crystal length (i.e., along the growth direction) as determined by XRF is illustrated in Fig. 1b; it indicates a slight variation across the ingot length. The composition of the samples used for XPD is given in Table 1.

The XPD patterns for the surfaces of these three crystals obtained by cleaving in UHV are presented in Fig. 2a-c. One can immediately notice the striking difference in the XPD patterns of Se and Te, especially in the central part, due to essentially different local structures. The calculated patterns for individual lattice positions are presented in Fig. 3; their initial comparison with the experimental observations indeed reveals preferential Se occupation of the Ch (1) site while Te is dominantly in the Ch (2) positions. For further quantification, we performed the XPD modeling. The EDAC simulation shows the preferential occupation of the Ch (2) position by Se, although the ideal tetradymite structure does not yield the best description of the experimental data. In our model, we admitted a mixed occupancy of the Ch (1) and Ch (2) positions and optimized the respective ordering factor within the formalism described above while also imposing constraints on the total composition (as obtained from the XRF data). The results are presented in Fig. 1d for one of the compositions. The *R*-factor dependence on the ordering factor has a distinct minimum in all cases. For all compositions, certain disordering is observed (see Table 1); this does not contradict the available early XPD and XRD/Rietveld data described in the Introduction section [23,36]. Fig. 2(e-f) clearly shows that the ordering increases with the Se content increase. At a low Se content (sample with *x*≈0.1), the Sb-Ch(2)-Sb distance is mostly defined by the atomic size of Te, since it dominates. This may lead to a smaller energy benefit for Se atoms to occupy the intralayer Ch(2) position.

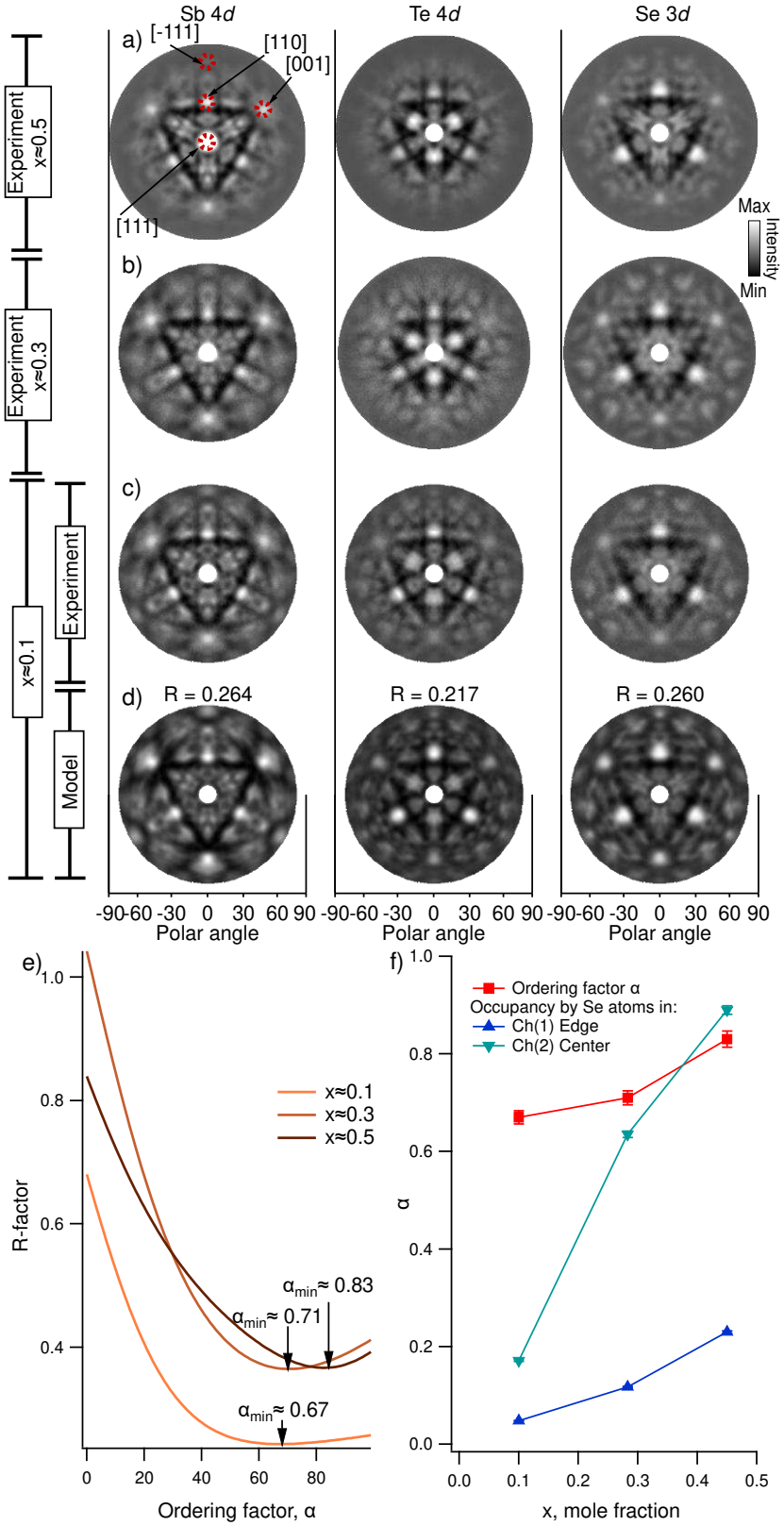

Fig. 2. (a-c) Azimuthal projections of experimental XPD patterns obtained for the $Sb_2(Te_{1-x}Se_x)_3$ crystals at an electron kinetic energy of 600 eV for Sb 4d (left), Se 3d (middle), and Te 4d (right), for different compositions marked on the left, (d) the optimal simulated XPD pattern for composition x≈0.1 with the corresponding R-factor values. (The same for x≈0.3 and x≈0.5 can be found in the Supplementary materials (Section 2), (e) the dependence of the R-factor on the ordering factor α, (f) the dependence of the ordering factor and occupancies of Ch positions by Se atoms on selenium mole fraction (x).

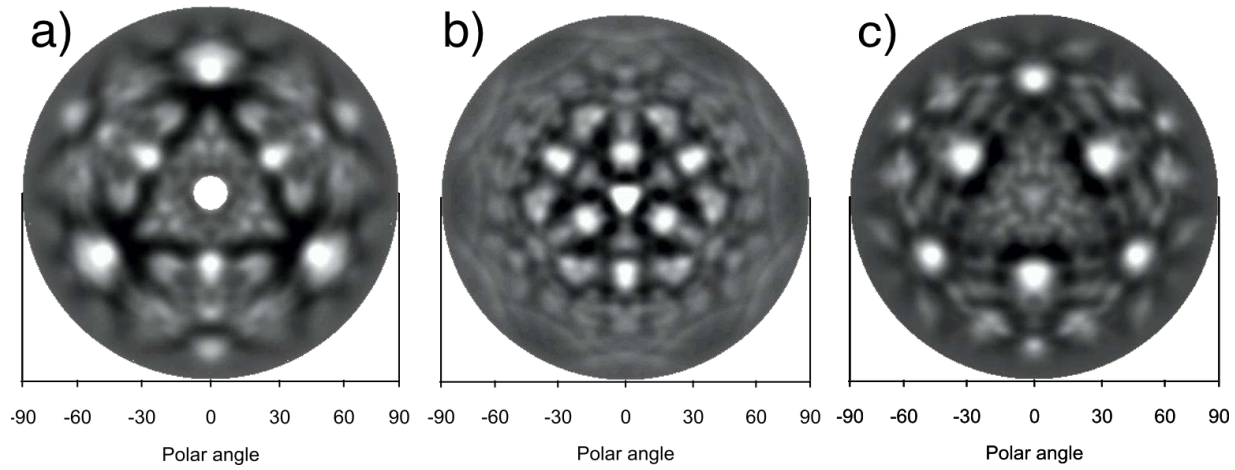

Fig. 3. Azimuthal projections of theoretical photoelectron diffraction patterns from different atomic sites. a) Sb, b) Ch (1), c) Ch (2).

For comparison with well-established experimental methods of atomic occupancy analysis, we also studied these samples by HAADF STEM/EDX. The total concentrations were determined by SEM-EDX as presented in Table 1. From the HAADF-STEM image of the sample with x≈0.5 in Fig. 4c, it is already clear that the Se atoms preferentially substitute the middle Te layer in the quintuple layer due to the Z contrast in the HAADF-STEM images. Se has a Z number of 34, while for Te Z=52, therefore, the columns that contain more Se atoms will appear darker than the columns with more Te atoms. No interstitial defects were observed in this experiment.

Table 1. Summary of the position occupancy analysis for $Sb_2(Te_{1-x}Se_x)_3$. The STEM/EDX occupancy of the Sb sites in all cases are equal to 100%.

SAMPLE	x≈0.1						x≈0.3						x≈0.5			
TOTAL COMPOSITION (EDX)	$Sb_{2.07(3)}(Se_{0.09(2)}Te_{0.89(1)})_3$						$Sb_{2.01(4)}(Se_{0.33(3)}Te_{0.67(2)})_3$						$Sb_{2.05(4)}(Se_{0.52(3)}Te_{0.47(2)})_3$			
TOTAL COMPOSITION (XRF)	$Sb_2(Se_{0.089(6)}Te_{0.912(6)})_3$						$Sb_2(Se_{0.290(6)}Te_{0.710(6)})_3$						$Sb_2(Se_{0.450(6)}Te_{0.550(6)})_3$			
TOTAL COMPOSITION (XRD)	Vegard's law: $Sb_2(Se_{0.0694(2)}Te_{0.9306(2)})_3$						Vegard's law: $Sb_2(Se_{0.2778(2)}Te_{0.7222(2)})_3$						Vegard's law: $Sb_2(Se_{0.4252(1)}Te_{0.5748(1)})_3$			
ATOMIC SITE OCCUPANCY	STEM/EDX		XPD/XRF		XRD/Rietveld		STEM/EDX		XPD/XRF		XRD/Rietveld		XPD/XRF		XRD/Rietveld	
	Te	Se	Te	Se	Te	Se	Te	Se	Te	Se	Te	Se	Te	Se	Te	Se
Ch(1)	94.0(6)	6.0(6)	95.2	4.8	92.6(2)	7.4(2)	86(2)	14(2)	88.3	11.7	94.7(2)	5.3(2)	77.0	23.0	79.5(2)	20.7(2)
Ch(2)	81.0(2)	19.0(2)	82.9	17.1	87.7(6)	12.3(6)	30(3)	70(3)	36.5	63.5	30.0(2)	70.0(2)	11.0	89.0	6.0(4)	93.7(4)
α	**0.61**		**0.67**		**0.45**		**0.71**		**0.71**		**0.87**		**0.83**		**0.94**	

We performed a more detailed EDX investigation with an atomic layer resolution to obtain a rough estimate for the occupancy of the structurally different Te/Se positions. We followed a similar procedure as described by Lu *et al.* [45,46], using the Sb-*L* (6.603 keV), Te-*L* (3.767 keV), and Se-*K* (11.210 keV) lines. In Fig. 4 the atomically resolved EDX maps of two samples are presented, where the averaged Se maps for x≈0.1 and x≈0.3 indicate that the outer layers of the QL layer contain Se. Therefore, upon gradual Te substitution with Se in the mixed crystals of $Sb_2(Te_{1-x}Se_x)_3$, the Se atoms are already present in the outer layers (i.e. in the Ch (1) positions) before the middle layer is completely filled by Se, which agrees well with our XPD data on the statistical distribution of chalcogen atoms for x≈0.1 but contradicts the data obtained from Ref. [23].

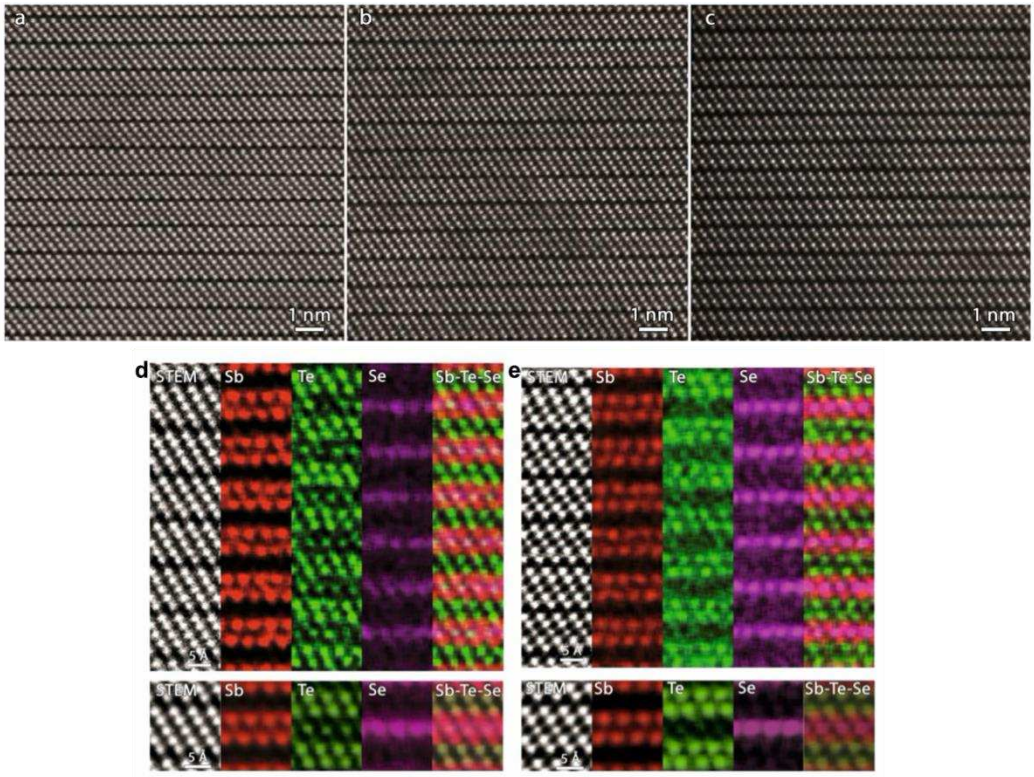

Fig. 4. (a-c) HAADF-STEM images of zone [010] for the $Sb_2(Se_xTe_{1-x})_3$ samples with x≈0.1(a), x≈0.3(b), and x≈0.5(c). (d-e) Atomically resolved EDX maps of the $Sb_2(Te_{1-x}Se_x)_3$ samples with x≈0.1(d) and x≈0.3(e) (See Supplementary materials, Section 4 for more details). The small EDX maps at the bottom of (d-e) were obtained from the top EDX map by averaging over different quintuple layers.

Quantitative analysis was performed by comparing the HAADF-STEM simulations with the experimental observations using the total concentrations obtained by EDX with the averaged experimental HAADF-STEM image presented in Fig. 5. The corresponding position occupancies are given in Table 1. They are in reasonable agreement with our XPD data. One can notice from Table 1, though, that both sets of the ordering factor values (XPD and HAADF-STEM/EDX) poorly agree with the respective Rietveld refined powder XRD results. A detailed description of the Rietveld refinement procedure that we followed and the results obtained are given in the Supplementary Materials (Section 3). Earlier, it has been demonstrated for different materials that the occupancies derived from HAADF-STEM/EDX (HAADF-STEM/EELS) and powder XRD after Rietveld refinement often differ, which is explained by most researchers by the locality of STEM compared to XRD [45–47]. The volume of matter probed by STEM is indeed by 7-8 orders of magnitude less than that for XPD; for XRD, it is 7-8 orders of magnitude more than for XPD and therefore up to 16 orders of magnitude higher than for STEM. However, the fact that XPD and HAADF-STEM/EDX data agree well, while the Rietveld-refined XRD results deviate remarkably, suggests that methods that are more chemically sensitive evidently yield more reliable data on the occupancies and ordering factors, thus the approach mentioned in the Introduction section, when the HAADF-STEM/EDX or HAADF-STEM/EELS data are used as a starting point for the occupancy determination by Rietveld refined XRD [27,28], seems to be more correct (as compared to the direct occupancy determination from the XRD data). We believe that the reason for this is that in mixed crystals with relatively high statistical disordering the ADP parameters during Rietveld refinement reflect the static displacement of the atoms rather than their dynamic motion; therefore, when the site occupancies and ADPs are refined simultaneously, there is often divergence in the resulting solution. This may also explain why the occupancies defined from XRD/Rietveld for x≈0.5 (a more ordered system) are closer to those

obtained with other methods compared to the data for $x \approx 0.1$ or $x \approx 0.3$ (i.e., the higher the ordering, the better the agreement between the methods).

It should be noted that the quality of the experimental X-ray photoelectron diffraction patterns observed for Te 4d for both $x \approx 0.3$ and $x \approx 0.5$ is worse than that for $x \approx 0.1$. This is not only due to lower Te concentration but might also be due to an XPD surface sensitivity issue. The main contributing factor is that in the third atomic layer from the surface the Te content becomes negligible due to its preferential substitution by Se. The first layer gives predominantly forward scattering, which is not so well modeled within the EDAC formalism, whereas the fifth layer yields weak intensity in the XPD patterns due to a low inelastic mean free path of electrons at a kinetic energy of 600 eV. In this case, more precise results can be potentially obtained using a significantly higher electron kinetic energy, however, such conditions have not been available for our experiments.

All in all, XPD yields the correct determination of the site occupancies and reproduces the HAADF STEM/EDX data. At the same time, the XPD data come generally from the very surface layers with variable surface sensitivity. For the surfaces obtained by cleavage, the surface composition, and the occupancies are generally not at equilibrium but are “frozen” as in the bulk. However, for natural surfaces like those of epitaxial films, there may be a substantial difference. In this case, XPD provides a unique opportunity to investigate the material structure.

In our case, we did not study thin films but, remarkably, the samples themselves contain flat voids, i.e. 3D defects of different volumes. The corresponding examples are presented in Fig. 6. These 3D defects still show the quintuple layer in projection, but with a darker contrast, while the EDX data in Fig. 6 show a decrease in Sb, Te, and Se content while no other chemical element is present. Therefore, the decrease in intensity is observed due to missing atomic clusters (probably discs). This suggests that the contrast difference is caused by a decrease in thickness and not by a change in chemical composition. Another explanation could be that the 3D defects are caused by the FIB sample preparation, however, no reports have been found in the literature regarding any similar defects caused by FIB for any other materials. Furthermore, such defects were also not present in any of the other samples that we investigated, which were all prepared with similar sample preparation settings. Another suggestion is that oxygen is captured in these areas. For example, oxygen might be present in the sample when the raw bulk Sb, Se, or Te material used for sample preparation was oxidized. However, in this case, the question remains why the void only consists of a single quintuple layer. Wu et al. [48] observed vacancy clusters in $(GeTe)_{0.975}(Bi_2Te_3)_{0.025}$, however, their specific size was not mentioned. Another proposition is that these materials contained another phase consisting for example only of Se, which is the lightest of the three elements. Due to the different structural properties between the two phases, the respective milling effect can be different, thus causing the removal of the extra phase by FIB. However, such a big difference in milling at such a local scale appears to be highly unlikely. Another possible explanation can be annealing, which was reported to be capable of removing secondary phases [49], however, no annealing after the sample preparation was performed on the investigated samples. So, the origin of these 3D defects, which appear as partial removal of one quintuple layer in the depth of the material, remains unclear. But, remarkably, the lattice position occupancy near the voids presenting the “internal surfaces” is rather different from that in the bulk. One can expect a similar effect for the surfaces formed naturally (e.g. during thin film growth), or for surfaces that have reached equilibrium upon cleavage, therefore XPD will evidently be a useful tool to probe such systems.

Having shown the different distributions between the anion positions within the quintuple layers as compared to the bulk, the question remains how the change in stoichiometry affects the topology of the system. In this material class, the topological phase transition is accessed by increasing the spin-orbit coupling strength, eventually leading to a band inversion and the emergence of topological surface states.

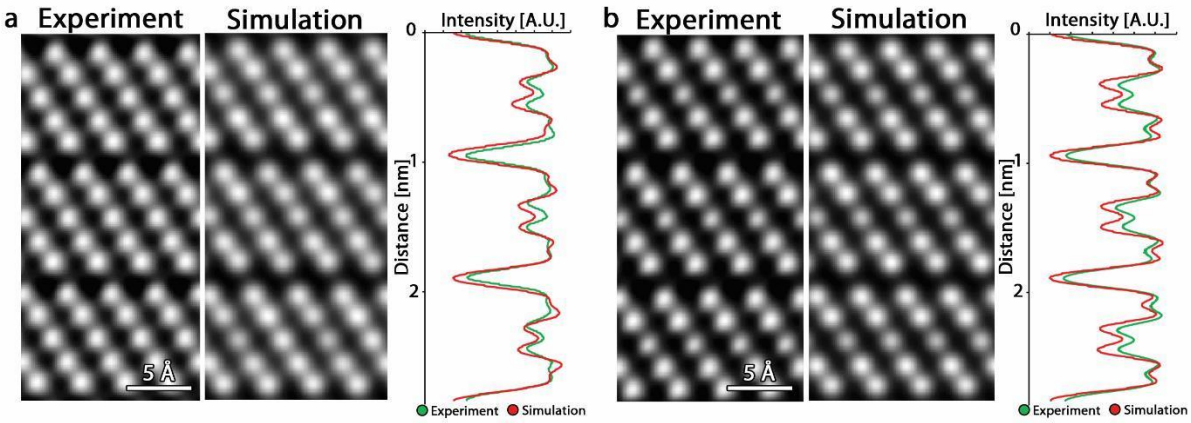

Fig. 5. Comparison between the averaged experimental HAADF-STEM images and the simulated HAADF-STEM images calculated using QSTEM [41] using the layer composition obtained by EDX and displayed in Table 1, and the corresponding line profiles for the $Sb_2(Te_{1-x}Se_x)_3$ samples with x≈0.1(a) and x≈0.3(b).

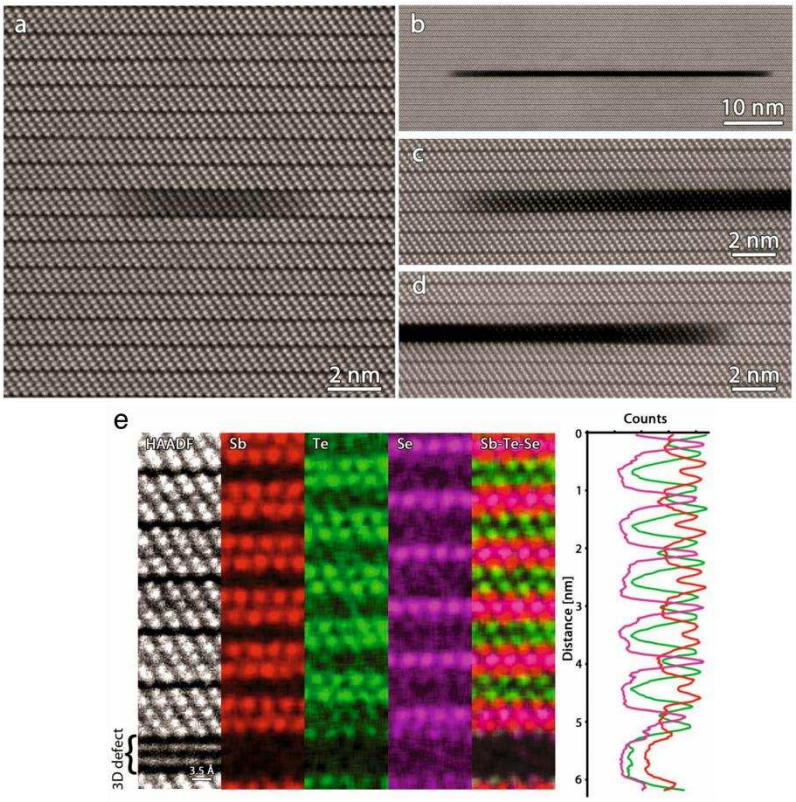

Fig. 6. HAADF-STEM images of the 3D defects in the $Sb_2(Te_{1-x}Se_x)_3$ sample with x≈0.1: (a),(b) An overview of two 3D defects of different size; (c), (d) Close-ups of the edges of the 3D defect from (b). e) EDX maps of zone [010] from the $Sb_2(Te_{1-x}Se_x)_3$ sample with x≈0.3 and a vertical line profile: Se occupies predominantly the central layer of the QL, but is also present in the outer layers. The EDX signals of Sb, Se, and Te drop at the location of the 3D defect.

Therefore, starting from the topologically non-trivial Sb_2Te_3, increasing Se incorporation will smoothly drive the system through the critical point back to the topologically trivial regime of Sb_2Se_3. To assess whether this transition has been surpassed for the case of the maximal investigated Se fraction (which also corresponds to the highest ordering, x=0.5), we investigated the electronic structure of $Sb_2(Te_{0.5}Se_{0.5})_3$ along with the topologically non-trivial parent compound Sb_2Te_3. Figure 7(a-b) shows the respective energy-momentum dispersions as probed by angle-resolved photoemission spectroscopy (ARPES), using 6 eV photons from a femtosecond (fs) laser source. Due to *p*-type doping in our samples, the topological surface state is out of reach in conventional ARPES experiments, which only probe the occupied states below the Fermi level (E_F).

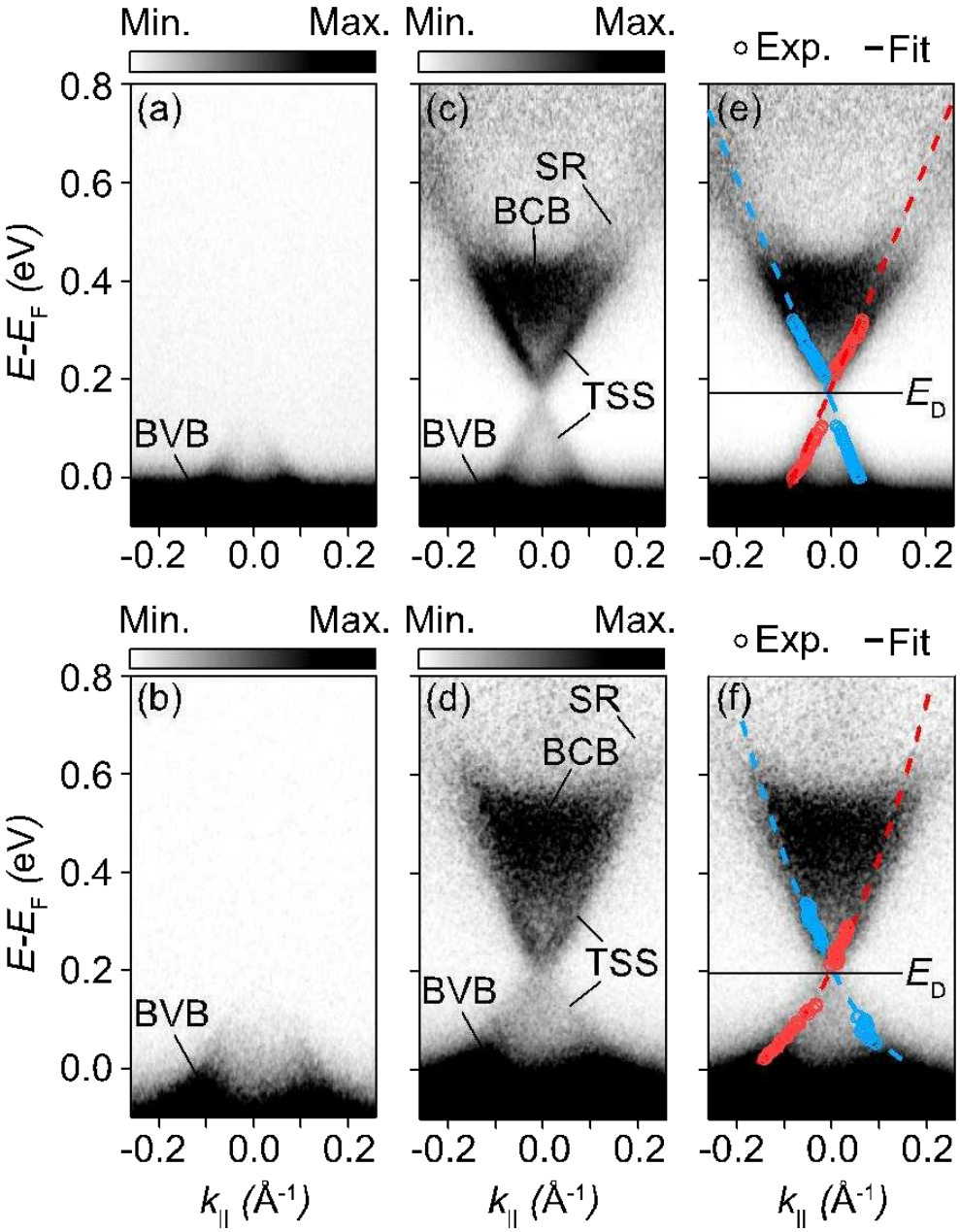

Fig. 7. (a-b) Electronic structure of Sb_2Te_3 (a)and $Sb_2(Te_{0.5}Se_{0.5})_3$ (b) as seen with conventional angle-resolved photoemission (ARPES) using 6 eV photons. The bulk valence bands (BVBs) are labeled. (c-d) Equivalent ARPES spectra following a transient population of the unoccupied states with a fs-laser 1.5 eV pump pulse. The topological surface state (TSS), surface resonance states (SR), and the bulk conduction band (BCB) are indicated for each compound. (e-f) The spectra from (c-d) are reproduced along with Lorentzian peak positions of the TSS dispersion (open circles). Dashed lines are fits to the overall TSS band dispersion for each compound. Red and blue colors indicate opposite spin states of the surface localized bands.

To overcome this issue, we transiently populated the unoccupied part of the band structure using a fs infrared laser pulse ($h\nu$=1.5 eV) in addition to the 6 eV fs probe, as shown in Fig. 7(c,d). Indeed, as shown in Fig. 7c, the band inversion and the topological surface state (TSS) are clearly seen for Sb_2Te_3 following optical excitation, as expected. Fig. 7d shows an equivalent energy-momentum region for $Sb_2(Te_{0.5}Se_{0.5})_3$, demonstrating that the topological surface state persists, unambiguously confirming that the system remains topologically non-trivial despite the reduction of the chalcogen derived spin-orbit coupling strength.

There are more subtle changes to the surface band dispersion, however. Whereas the TSS in Sb_2Te_3 adopts a shape that is well approximated by a strictly linear band dispersion over an extended region away from the crossing point (dashed lines in Fig. 7e), the TSS in $Sb_2(Te_{0.5}Se_{0.5})_3$ deviates substantially from linearity, requiring higher-order terms to well approximate the extracted band dispersion (dashed lines in Fig. 7f). This deviation is coupled to an increased effective mass corresponding to a reduction in the group velocity

of the TSS bands by a factor of 0.82. This observation is consistent with a narrowing of the inverted bandgap as Se is incorporated, despite the small shift of the Dirac point energy (E_D) by ~30 meV.

Therefore, the present results on anion substituted $Sb_2(Se,Te)_3$ chalcogenides are of fundamental importance to the topological insulator material class.

4. Conclusions

We found that the XPD data on the occupancies of lattice positions for the surfaces obtained from bulk crystals by cleaving under UHV are in good agreement with the HAADF-STEM/EDX observations used as a reference to probe the bulk positions. Using both approaches, we revealed that in the range of $Sb_2(Te_{1-x}Se_x)_3$ compositions between $x\approx0.1$ and $x\approx0.5$ the ordering increases with the Se fraction increase, and demonstrated that both methods are better suited to describe the occupancies in mixed crystals than the currently more widespread powder XRD with Rietveld refinement, which has uncertainty related to hardly separable contributions of occupancy and atomic displacement parameters.
We also revealed that the anionic occupancy near rarely observed crystal defects – voids - is quite different from that in the bulk. This suggests that naturally formed surfaces (for example, those of thin films) can show significantly different anion distribution between the anion positions within the quintuple layers as compared to the bulk or to surfaces formed in the UHV from single crystals by cleavage. In the case of naturally formed surfaces, XPD is currently the only method to probe this issue. Finally, by directly probing the transiently occupied energy-momentum dispersion of topological surface states above the Fermi level following ultrafast optical excitation, we have shown that the present results on anion substituted $Sb_2(Te_{1-x}Se_x)_3$ chalcogenides are of fundamental importance to the topological insulator material class.

Acknowledgments

We acknowledge financial support from the Russian Science Foundation (RSF) under grant No. 19-42-06303, and the Impuls- und Vernetzungsfonds der Helmholtz-Gemeinschaft under grant No. HRSF-0067 (Helmholtz-Russia Joint Research Group). N.V.V., A.S.F. and D.Yu.U acknowledged the support of RSF grant 22-72-10074 and strategic academic leadership program «Priority 2030» (Agreement 075-02-2021-1316 from 30.09.2021)We also acknowledge the Paul Scherrer Institut, Villigen, Switzerland, for the provision of synchrotron beamtime at the PEARL beamline of the Swiss Light Source for the XPD measurements. N.V.V. acknowledges the individual support grant of the RFBR (No. 20-33-90273) for her PhD studies (crystal growth and characterization). J.H. and C.C. acknowledge the support from the University of Antwerp through BOF Grant No. 31445.

References

[1] J.E. Moore, The birth of topological insulators, Nature. 464 (2010) 194–198. https://doi.org/10.1038/nature08916.
[2] B.A. Bernevig, T.L. Hughes, S.-C. Zhang, Quantum Spin Hall Effect and Topological Phase Transition in HgTe Quantum Wells, Science. 314 (2006) 1757–1761. https://doi.org/10.1126/science.1133734.
[3] M. Koenig, S. Wiedmann, C. Bruene, A. Roth, H. Buhmann, L.W. Molenkamp, X.-L. Qi, S.-C. Zhang, Quantum Spin Hall Insulator State in HgTe Quantum Wells, Science. 318 (2007) 766–770. https://doi.org/10.1126/science.1148047.
[4] D.-X. Qu, Y.S. Hor, J. Xiong, R.J. Cava, N.P. Ong, Quantum Oscillations and Hall Anomaly of Surface States in the Topological Insulator Bi2Te3, Science. 329 (2010) 821–824. https://doi.org/10.1126/science.1189792.
[5] Z. Ren, A.A. Taskin, S. Sasaki, K. Segawa, Y. Ando, Optimizing Bi2-xSbxTe3-ySey solid solutions to approach the intrinsic topological insulator regime, Phys Rev B. 84 (2011) 165311. https://doi.org/10.1103/physrevb.84.165311.

[6] T. Arakane, T. Sato, S. Souma, K. Kosaka, K. Nakayama, M. Komatsu, T. Takahashi, Z. Ren, K. Segawa, Y. Ando, Tunable Dirac cone in the topological insulator Bi2-xSbxTe3-ySey, Nat Commun. 3 (2012) 636. https://doi.org/10.1038/ncomms1639.
[7] A.A. Taskin, Z. Ren, S. Sasaki, K. Segawa, Y. Ando, Observation of Dirac Holes and Electrons in a Topological Insulator, Phys Rev Lett. 107 (2011) 016801. https://doi.org/10.1103/physrevlett.107.016801.
[8] S. Jia, H. Ji, E. Climent-Pascual, M.K. Fuccillo, M.E. Charles, J. Xiong, N.P. Ong, R.J. Cava, Low-carrier-concentration crystals of the topological insulator Bi2Te2Se, Phys Rev B. 84 (2011) 235206. https://doi.org/10.1103/physrevb.84.235206.
[9] A. Kadhim, A. Hmood, H.A. Hassan, Thermoelectric generation device based on p-type Bi0.4Sb1.6Te3 and n-type Bi2Se0.6Te2.4 bulk materials prepared by solid state microwave synthesis, Solid State Commun. 166 (2013) 44–49. https://doi.org/10.1016/j.ssc.2013.04.020.
[10] H. Ji, J.M. Allred, M.K. Fuccillo, M.E. Charles, M. Neupane, L.A. Wray, M.Z. Hasan, R.J. Cava, Bi2Te1.6S1.4: A topological insulator in the tetradymite family, Phys Rev B. 85 (2012) 201103. https://doi.org/10.1103/physrevb.85.201103.
[11] Z. Ren, A.A. Taskin, S. Sasaki, K. Segawa, Y. Ando, Large bulk resistivity and surface quantum oscillations in the topological insulator Bi2Te2Se, Phys Rev B. 82 (2010) 241306. https://doi.org/10.1103/physrevb.82.241306.
[12] S.-M. Huang, S.-H. Yu, M. Chou, The linear magnetoresistance from surface state of the Sb2SeTe2 topological insulator, J Appl Phys. 119 (2016) 245110. https://doi.org/10.1063/1.4954290.
[13] S.-M. Huang, S.-J. Huang, Y.-J. Yan, S.-H. Yu, M. Chou, H.-W. Yang, Y.-S. Chang, R.-S. Chen, Highly responsive photoconductance in a Sb 2 SeTe 2 topological insulator nanosheet at room temperature, Rsc Adv. 7 (2017) 39057–39062. https://doi.org/10.1039/c7ra06151j.
[14] S.-M. Huang, S.-J. Huang, Y.-J. Yan, S.-H. Yu, M. Chou, H.-W. Yang, Y.-S. Chang, R.-S. Chen, Extremely high-performance visible light photodetector in the Sb2SeTe2 nanoflake, Sci Rep-Uk. 7 (2017) 45413. https://doi.org/10.1038/srep45413.
[15] S.-M. Huang, Y.-J. Yan, S.-H. Yu, M. Chou, Thickness-dependent conductance in Sb2SeTe2 topological insulator nanosheets, Sci Rep-Uk. 7 (2017) 1896. https://doi.org/10.1038/s41598-017-02102-7.
[16] E. Papalazarou, L. Khalil, M. Caputo, L. Perfetti, N. Nilforoushan, H. Deng, Z. Chen, S. Zhao, A. Taleb-Ibrahimi, M. Konczykowski, A. Hruban, A. Wołoś, A. Materna, L. Krusin-Elbaum, M. Marsi, Unraveling the Dirac fermion dynamics of the bulk-insulating topological system Bi2Te2Se, Phys Rev Mater. 2 (2018) 104202. https://doi.org/10.1103/physrevmaterials.2.104202.
[17] Y.E. Khatchenko, M.V. Yakushev, C. Seibel, H. Bentmann, M. Orlita, V. Golyashov, Y.S. Ponosov, N.P. Stepina, A.V. Mudriy, K.A. Kokh, O.E. Tereshchenko, F. Reinert, R.W. Martin, T.V. Kuznetsova, Structural, optical and electronic properties of the wide bandgap topological insulator Bi1.1Sb0.9Te2S, J Alloy Compd. 890 (2022) 161824. https://doi.org/10.1016/j.jallcom.2021.161824.
[18] S.-M. Huang, S.-H. Yu, M. Chou, The large linear magnetoresistance in Sb2Se2Te single crystal with extremely low mobility, Mater Res Express. 3 (2016) 126101. https://doi.org/10.1088/2053-1591/3/12/126101.
[19] K. Shrestha, V. Marinova, D. Graf, B. Lorenz, C.W. Chu, Large magnetoresistance and Fermi surface study of Sb 2 Se 2 Te single crystal, J Appl Phys. 122 (2017) 125901. https://doi.org/10.1063/1.4998575.
[20] Y. Liu, L.-L. Wang, Q. Zheng, Z. Huang, X. Wang, M. Chi, Y. Wu, B.C. Chakoumakos, M.A. McGuire, B.C. Sales, W. Wu, J. Yan, Site Mixing for Engineering Magnetic Topological Insulators, Phys Rev X. 11 (2021) 021033. https://doi.org/10.1103/physrevx.11.021033.
[21] S. Wimmer, J. Sánchez-Barriga, P. Küppers, A. Ney, E. Schierle, F. Freyse, O. Caha, J. Michalička, M. Liebmann, D. Primetzhofer, M. Hoffman, A. Ernst, M.M. Otrokov, G. Bihlmayer, E. Weschke, B. Lake, E.V. Chulkov, M. Morgenstern, G. Bauer, G. Springholz, O. Rader, Mn-Rich MnSb2Te4: A Topological Insulator with Magnetic Gap Closing at High Curie Temperatures of 45–50 K, Adv Mater. (2021). https://doi.org/10.1002/adma.202102935.
[22] T. Murakami, Y. Nambu, T. Koretsune, G. Xiangyu, T. Yamamoto, C.M. Brown, H. Kageyama, Realization of interlayer ferromagnetic interaction in MnSb2Te4 toward the magnetic Weyl semimetal state, Phys Rev B. 100 (2019) 195103. https://doi.org/10.1103/physrevb.100.195103.

[23] T.L. Anderson, H.B. Krause, Refinement of the Sb2Te3 and Sb2Te2Se structures and their relationship to nonstoichiometric Sb2Te3−ySey compounds, Acta Crystallogr Sect B Struct Crystallogr Cryst Chem. 30 (1974) 1307–1310. https://doi.org/10.1107/s0567740874004729.
[24] A. Zeugner, F. Nietschke, A.U.B. Wolter, S. Gaß, R.C. Vidal, T.R.F. Peixoto, D. Pohl, C. Damm, A. Lubk, R. Hentrich, S.K. Moser, C. Fornari, C.H. Min, S. Schatz, K. Kißner, M. Ünzelmann, M. Kaiser, F. Scaravaggi, B. Rellinghaus, K. Nielsch, C. Hess, B. Büchner, F. Reinert, H. Bentmann, O. Oeckler, T. Doert, M. Ruck, A. Isaeva, Chemical Aspects of the Candidate Antiferromagnetic Topological Insulator MnBi2Te4, Chem Mater. 31 (2019) 2795–2806. https://doi.org/10.1021/acs.chemmater.8b05017.
[25] E.D.L. Rienks, S. Wimmer, J. Sánchez-Barriga, O. Caha, P.S. Mandal, J. Růžička, A. Ney, H. Steiner, V.V. Volobuev, H. Groiss, M. Albu, G. Kothleitner, J. Michalička, S.A. Khan, J. Minár, H. Ebert, G. Bauer, F. Freyse, A. Varykhalov, O. Rader, G. Springholz, Large magnetic gap at the Dirac point in Bi2Te3/MnBi2Te4 heterostructures, Nature. 576 (2019) 423–428. https://doi.org/10.1038/s41586-019-1826-7.
[26] K. Adouby, M.L.E. Moubtassim, C.P. Vicente, J.C. Jumas, A.A. Touré, X-ray diffraction, 119Sn Mössbauer and thermal study of SnSe–Bi2Se3 system, J Alloy Compd. 453 (2008) 161–166. https://doi.org/10.1016/j.jallcom.2006.11.138.
[27] O.A. Tyablikov, D. Batuk, A.A. Tsirlin, M. Batuk, V.Yu. Verchenko, D.S. Filimonov, K.V. Pokholok, D.V. Sheptyakov, M.G. Rozova, J. Hadermann, E.V. Antipov, A.M. Abakumov, {110}-Layered B-cation ordering in the anion-deficient perovskite Pb 2.4 Ba 2.6 Fe 2 Sc 2 TiO 13 with the crystallographic shear structure, Dalton T. 44 (2015) 10753–10762. https://doi.org/10.1039/c4dt03867c.
[28] D.T. Alvarez-Ruiz, F. Azough, T. Slater, S.J. Day, R. Freer, The effect of nano-twins on the thermoelectric properties of Ga2O3(ZnO)m (m = 9, 11, 13 and 15) homologous compounds, J Eur Ceram Soc. 40 (2020) 5549–5558. https://doi.org/10.1016/j.jeurceramsoc.2020.07.021.
[29] C. Callaert, M. Bercx, D. Lamoen, J. Hadermann, Interstitial defects in the van der Waals gap of Bi2Se3, Acta Crystallogr Sect B. 75 (2019) 717–732. https://doi.org/10.1107/s2052520619008357.
[30] D.P. Woodruff, Photoelectron diffraction: Early demonstrations and alternative modes, J Vac Sci Technology Vac Surfaces Films. 39 (2021) 040801. https://doi.org/10.1116/6.0001104.
[31] A.A. Volykhov, J. Sánchez-Barriga, M. Batuk, C. Callaert, J. Hadermann, A.P. Sirotina, V.S. Neudachina, A.I. Belova, N.V. Vladimirova, M.E. Tamm, N.O. Khmelevsky, C. Escudero, V. Pérez-Dieste, A. Knop-Gericke, L.V. Yashina, Can surface reactivity of mixed crystals be predicted from their counterparts? A case study of (Bi 1−x Sb x) 2 Te 3 topological insulators, J Mater Chem C. 6 (2018) 8941–8949. https://doi.org/10.1039/c8tc02235f.
[32] J.P. Heremans, R.J. Cava, N. Samarth, Tetradymites as thermoelectrics and topological insulators, Nat Rev Mater. 2 (2017) 17049. https://doi.org/10.1038/natrevmats.2017.49.
[33] D. West, Y.Y. Sun, H. Wang, J. Bang, S.B. Zhang, Native defects in second-generation topological insulators: Effect of spin-orbit interaction on Bi2Se3, Phys Rev B. 86 (2012) 121201. https://doi.org/10.1103/physrevb.86.121201.
[34] V.I. Ivlieva, N.Kh. Abrikosov, Phase equilibrium in systems formed by antimony chalcogenides, Dokl. Akad. Nauk SSSR. 159 (1964) 1326–1329.
[35] A.A. Volykhov, A.S. Frolov, V.S. Neudachina, N.V. Vladimirova, E. Gerber, C. Callaert, J. Hadermann, N.O. Khmelevsky, A. Knop-Gericke, J. Sánchez-Barriga, L.V. Yashina, Impact of Ordering on the Reactivity of Mixed Crystals of Topological Insulators with Anion Substitution: Bi2SeTe2 and Sb2SeTe2, Appl Surf Sci. (2020) 148490. https://doi.org/10.1016/j.apsusc.2020.148490.
[36] R.L. Benbow, M.R. Thuler, Z. Hurych, K.H. Lau, S.Y. Tong, Photoelectron diffraction from layered Sb2Te2Se, Phys Rev B. 28 (1983) 4160–4168. https://doi.org/10.1103/physrevb.28.4160.
[37] S. Jia, H. Beidenkopf, I. Drozdov, M.K. Fuccillo, J. Seo, J. Xiong, N.P. Ong, A. Yazdani, R.J. Cava, Defects and high bulk resistivities in the Bi-rich tetradymite topological insulator Bi2+xTe2−xSe, Phys Rev B. 86 (2012) 165119. https://doi.org/10.1103/physrevb.86.165119.
[38] V.I. Shtanov, L.V. Yashina, On the Bridgman growth of lead–tin selenide crystals with uniform tin distribution, J Cryst Growth. 311 (2009) 3257–3264. https://doi.org/10.1016/j.jcrysgro.2009.03.031.
[39] I. Lobato, D.V. Dyck, MULTEM: A new multislice program to perform accurate and fast electron diffraction and imaging simulations using Graphics Processing Units with CUDA, Ultramicroscopy. 156 (2015) 9–17. https://doi.org/10.1016/j.ultramic.2015.04.016.

[40] C. Koch, Determination of core structure periodicity and point defect density along dislocations. Ph. D. Arizona State University, 2002.
[41] F.J.G. de Abajo, M.A.V. Hove, C.S. Fadley, Multiple scattering of electrons in solids and molecules: A cluster-model approach, Phys Rev B. 63 (2001) 075404. https://doi.org/10.1103/physrevb.63.075404.
[42] D.Yu. Usachov, A.V. Tarasov, K.A. Bokai, V.O. Shevelev, O.Yu. Vilkov, A.E. Petukhov, A.G. Rybkin, I.I. Ogorodnikov, M.V. Kuznetsov, M. Muntwiler, F. Matsui, L.V. Yashina, C. Laubschat, D.V. Vyalikh, Site- and spin-dependent coupling at the highly ordered h-BN/Co(0001) interface, Phys Rev B. 98 (2018) 195438. https://doi.org/10.1103/physrevb.98.195438.
[43] A. VERDINI, M. SAMBI, F. BRUNO, D. CVETKO, M.D. NEGRA, R. GOTTER, L. FLOREANO, A. MORGANTE, G.A. RIZZI, G. GRANOZZI, DETERMINATION OF TiO2(110) SURFACE RELAXATION BY VARIABLE POLARIZATION PHOTOELECTRON DIFFRACTION, Surf Rev Lett. 6 (1999) 1201–1206. https://doi.org/10.1142/s0218625x99001347.
[44] G.C. Gazzadi, P. Luches, A. di Bona, L. Marassi, L. Pasquali, S. Valeri, S. Nannarone, Structural analysis of Fe/Ni(001) films by photoelectron diffraction, Phys Rev B. 61 (1999) 2246–2253. https://doi.org/10.1103/physrevb.61.2246.
[45] T. Lunkenbein, F. Girgsdies, A. Wernbacher, J. Noack, G. Auffermann, A. Yasuhara, A. Klein-Hoffmann, W. Ueda, M. Eichelbaum, A. Trunschke, R. Schlögl, M.G. Willinger, Direct Imaging of Octahedral Distortion in a Complex Molybdenum Vanadium Mixed Oxide, Angew Chem-Ger Edit. 127 (2015) 6932–6935. https://doi.org/10.1002/ange.201502236.
[46] W.D. Pyrz, D.A. Blom, N.R. Shiju, V.V. Guliants, T. Vogt, D.J. Buttrey, Using Aberration-Corrected STEM Imaging to Explore Chemical and Structural Variations in the M1 Phase of the MoVNbTeO Oxidation Catalyst, J Phys Chem C. 112 (2008) 10043–10049. https://doi.org/10.1021/jp801584m.
[47] M. Kušter, A. Meden, B. Markoli, Z. Samardžija, M. Vončina, P. Boulet, É. Gaudry, J.-M. Dubois, S. Šturm, Crystal Structure, Microstructure and Electronic Properties of a Newly Discovered Ternary Phase in the Al-Cr-Sc System, Crystals. 11 (2021) 1535. https://doi.org/10.3390/cryst11121535.
[48] D. Wu, L. Xie, X. Xu, J. He, High Thermoelectric Performance Achieved in GeTe–Bi2Te3 Pseudo-Binary via Van der Waals Gap-Induced Hierarchical Ferroelectric Domain Structure, Adv Funct Mater. 29 (2019) 1806613. https://doi.org/10.1002/adfm.201806613.
[49] A.U. Khan, K. Kobayashi, D.-M. Tang, Y. Yamauchi, K. Hasegawa, M. Mitome, Y. Xue, B. Jiang, K. Tsuchiya, D. Golberg, Y. Bando, T. Mori, Nano-micro-porous skutterudites with 100% enhancement in ZT for high performance thermoelectricity, Nano Energy. 31 (2017) 152–159. https://doi.org/10.1016/j.nanoen.2016.11.016.

Supplementary Materials to:

Occupancy of lattice positions probed by X-ray photoelectron diffraction: A case study of tetradymite topological insulators

Nadezhda V. Vladimirova[1,2,3], Alexander S. Frolov[1,2,3], Jaime Sánchez-Barriga[4], Oliver J. Clark[4], Fumihiko Matsui[5], Dmitry Yu. Usachov[3,6], Matthias Muntwiler[7], Carolien Callaert[8], Joke Hadermann[8], Vera Neudachina[2], Marina E. Tamm[1], Lada V. Yashina[1,2]*

1) Lomonosov Moscow State University, Leninskie Gory 1/3, 119991 Moscow, Russia
2) N.N. Semenov Federal Research Center for Chemical Physics, Kosygina Street 4, 119991 Moscow, Russia
3) Center for Advanced Mesoscience and Nanotechnology, Moscow Institute of Physics and Technology, National Research University, 9 Institutskiy Pereulok, Dolgoprudny, Moscow Region 141700, Russia
4) Helmholtz-Zentrum Berlin für Materialien und Energie, Elektronenspeicherring BESSY II, Albert-Einstein-Str. 15, 12489 Berlin, Germany
5) Institute for Molecular Science, Okazaki 444-8585 Japan
6) St. Petersburg State University, 7/9 Universitetskaya nab., 199034 St. Petersburg, Russia
7) Laboratory for Micro- and Nanotechnology, Paul Scherrer Institute, 5232 Villigen PSI, Switzerland
8) EMAT, Department of Physics, University of Antwerp, Groenenborgerlaan 171, 2020 Antwerp, Belgium
*Corresponding author. E-mail: yashina@inorg.chem.msu.ru

Section 1. The effect of different scattering factors of chalcogen atoms on the scattering amplitudes in the XPD patterns

In our two-surface model (see the Methods section of the main text), we assume that the difference in the scattering factors for Se and Te atoms is negligible. This allows us to represent the diffraction pattern of a mixed crystal as a linear combination of its binary constituents.

Generally, a photoelectron diffraction pattern can be influenced by the scattering factor of atoms around the emitter [1]. To estimate the influence of different scattering factors of chalcogen atoms on the intensity of theoretical XPD patterns, we simulated images for two clusters, Sb_2Se_3(111) and Sb_2Te_3(111) (Fig. S1). All structural parameters (i.e., the crystal structure, the lattice parameters, and the atomic coordinates) as well as non-structural parameters were chosen to be equal. I.e., the only difference was the type of chalcogen atom in this simulation. The calculated *R*-factor of the simulated patterns was estimated as 0.036, thus confirming the correctness of our approximation.

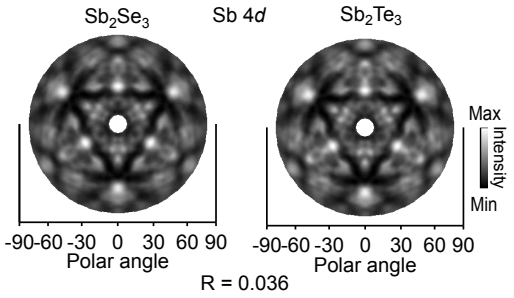

Fig. S1. Azimuthal projections of theoretical XPD patterns of Sb 4d photoemission peak for two clusters, Sb_2Te_3(111) (left) and Sb_2Se_3(111) (right). Both simulations were performed for an electron kinetic energy KE=600 eV in equal conditions (structural and non-structural parameters). Note the low R-factor value.

Section 2. The XPD patterns for $Sb_2(Te_{1-x}Se_x)_3$, x≈0.5 and x≈0.3

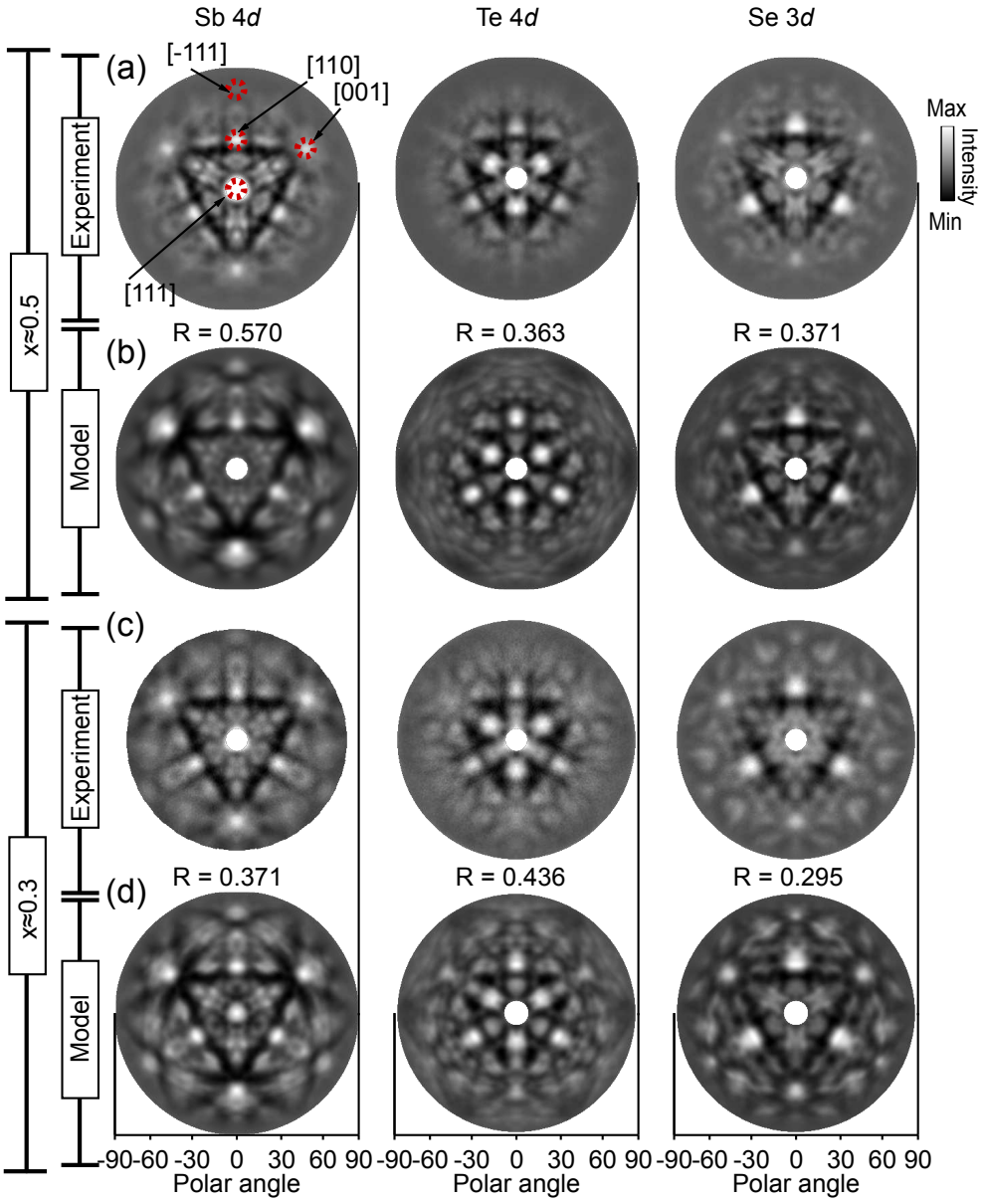

Fig. S2. Azimuthal projections of experimental (a,c) and the optimal simulated (b,d) XPD patterns obtained for the $Sb_2(Te_{1-x}Se_x)_3$ crystals at an electron kinetic energy of 600 eV for Sb 4d (left), Se 3d (middle), and Te 4d (right) with the corresponding R-factor values.

Section 3. Rietveld refinement of the powder XRD data

Both Sb_2Te_3 and $Sb_2(Te_{1-x}Se_x)_3$ (x≈0.1, 0.3 and 0.5) have a rhombohedral structure with the space group $R\bar{3}m$ (No. 166) [2]. To find the lattice constants, the zero shift was determined by adding powdered elemental germanium as an internal standard. With the increase of x the a and c parameters decrease,

which in turn leads to preferable occupation of the Ch (2) chalcogen sites by selenium as its ionic and covalent radii are shorter than those of tellurium (r_{ion}(Se)=0.198 nm, r_{cov}(Se)=0.120(4) nm; while r_{ion}(Te)=0.221, r_{cov}(Te)=0.138(4)). Powders made from layered crystals are strongly textured, and to reduce the texturing effect, the XRD samples were prepared by putting the corresponding powders on top of a glass sample holder coated with a thin layer of petroleum jelly. The resulting samples were free of any preferential texturing, according to the obtained powder XRD data.

The structural refinements were performed by the Rietveld method. The X-ray powder patterns were fitted using a Jana 2006 analysis program to minimize the profile discrepancy factor. The structure was refined in the $R\bar{3}m$ trigonal space group, in which Te atoms were located at sites 6*c*, which correspond to Ch (1), Sb atoms were at sites 6*c*, which correspond to the cation positions in this structure, and Se atoms (as well as partially Te atoms in case of x≈0.1) were at sites 3*a*, which correspond to Ch (2). To determine the position occupancies, we used anisotropic displacement factors (ADFs) solved for Sb_2Te_3 by Serrano-Sánchez F. et al [2] with subsequent refinement of the ADF values after initial determination of the occupancies. The refined ADF values coincide with those in [2] within the error limits. The occupancies of the chalcogen positions, Ch (1) and Ch (2), were refined since it was already mentioned above that substitution takes place at both chalcogen sites in the same time. For all $Sb_2(Te_{1-x}Se_x)_3$ compositions considered in our paper (x≈0.1, 0.3 and 0.5), the occupancy parameters were refined with the following constrains:

$$occ(Te\ (1)) = 1-x - occ(Te\ (2)),$$
$$occ(Se\ (1)) = x - occ(Se\ (2)),$$
$$occ(Ch\ (1)) = occ(Te\ (1)) + occ(Se\ (1)) = 1,$$
$$occ(Ch\ (2)) = occ(Te\ (2)) + occ(Se\ (2)) = 1.$$

The resulting compositions obtained from the Rietveld refinement are presented in Table 1 of the main text. Table S1 below lists the refinement conditions, the cell parameters, and the respective reliability factors; Table S2 shows the resulting data for the atomic coordinates and Table S3 lists the resulting ADF values. Figure S3 shows the calculated and the observed diffraction profiles.

Table S1. The conditions of Rietveld refinement (from the X-ray powder data) for $Sb_2(Te_{1-x}Se_x)_3$.

		x≈0.1	x≈0.3	x≈0.5
Wavelength (Å)		$\lambda k\alpha_1$=1.540593, $\lambda k\alpha_2$=1.544427; I($k\alpha_1$)/I($k\alpha_2$)=0.497		
Temperature		298 K		
2θ range (°)		10 - 82		
Step scan increment (°2θ)		0.02		
Zero point (°2θ)		0.0924(5)	0.0979(5)	0.0600(3)
Lattice parameters:		Space group: $R\bar{3}m$, *a* = *b*, α = β = 90°, γ = 120°		
	a (Å)	4.24600(5)	4.19494(5)	4.15885(3)
	c (Å)	30.3459(6)	29.9856(5)	29.7861(4)
	V (Å^3)	473.80(1)	456.98(1)	446.160(6)
	χ^2	2.36	2.44	2.82

Rp	2.23	2.28	2.67
wRp	3.77	3.88	4.21

Table S2. The refined structural parameters for $Sb_2(Te_{1-x}Se_x)_3$

	Wyckoff site	Site symmetry	x	y	z	Occupancy
x≈0.1						
Sb1	6c	3m	0	0	0.39769(3)	1.000
Ch (1): Te1	6c	3m	0	0	0.21297(2)	0.926(2)
Se1	6c	3m	0	0	0.21297(2)	0.074(2)
Ch (2): Te2	3a	$\bar{3}m$	0	0	0	0.877(7)
Se2	3a	$\bar{3}m$	0	0	0	0.123(7)
x≈0.3						
Sb1	6c	3m	0	0	0.39439(3)	1.009(8)
Ch (1): Te1	6c	3m	0	0	0.21428(3)	0.947(2)
Se1	6c	3m	0	0	0.21428(3)	0.053(2)
Ch (2): Te2	3a	$\bar{3}m$	0	0	0	0.300(7)
Se2	3a	$\bar{3}m$	0	0	0	0.700(7)
x≈0.5						
Sb1	6c	3m	0	0	0.39439(2)	1.001(2)
Ch (1): Te1	6c	3m	0	0	0.21486(2)	0.795(2)
Se1	6c	3m	0	0	0.21486(2)	0.207(2)
Ch (1): Te2	3a	$\bar{3}m$	0	0	0	0.060(4)
Se2	3a	$\bar{3}m$	0	0	0	0.937(4)

Table S3. The refined ADF values for $Sb_2(Te_{1-x}Se_x)_3$.

	U_{11}	U_{22}	U_{33}	U_{12}	U_{13}	U_{23}
x≈0.1						
Sb1	0.021(3)	0.021(3)	0.033(4)	0.014(3)	0	0
Ch (1): Te1	0.020(4)	0.020(4)	0.022(3)	0.010(4)	0	0

Se1	0.020(4)	0.020(4)	0.022(3)	0.010(4)	0	0
Ch (2): Te2	0.024(1)	0.024(1)	0.01(1)	0.012(1)	0	0
Se2	0.024(1)	0.024(1)	0.01(1)	0.012(1)	0	0
x≈0.3						
Sb1	0.017(1)	0.017(1)	0.033(4)	0.009(1)	0	0
Ch (1): Te1	0.017(1)	0.017(1)	0.022(3)	0.009(1)	0	0
Se1	0.017(1)	0.017(1)	0.022(3)	0.009(1)	0	0
Ch (2): Te2	0.020(2)	0.020(2)	0.008(4)	0.011(1)	0	0
Se2	0.020(2)	0.020(2)	0.008(4)	0.011(1)	0	0
x≈0.5						
Sb1	0.021(3)	0.021(3)	0.033(4)	0.011(3)	0	0
Ch (1): Te1	0.020(4)	0.020(4)	0.022(3)	0.010(4)	0	0
Se1	0.020(4)	0.020(4)	0.022(3)	0.010(4)	0	0
Ch (2): Te2	0.018(5)	0.018(5)	0.008(4)	0.010(4)	0	0
Se2	0.018(5)	0.018(5)	0.008(4)	0.010(4)	0	0

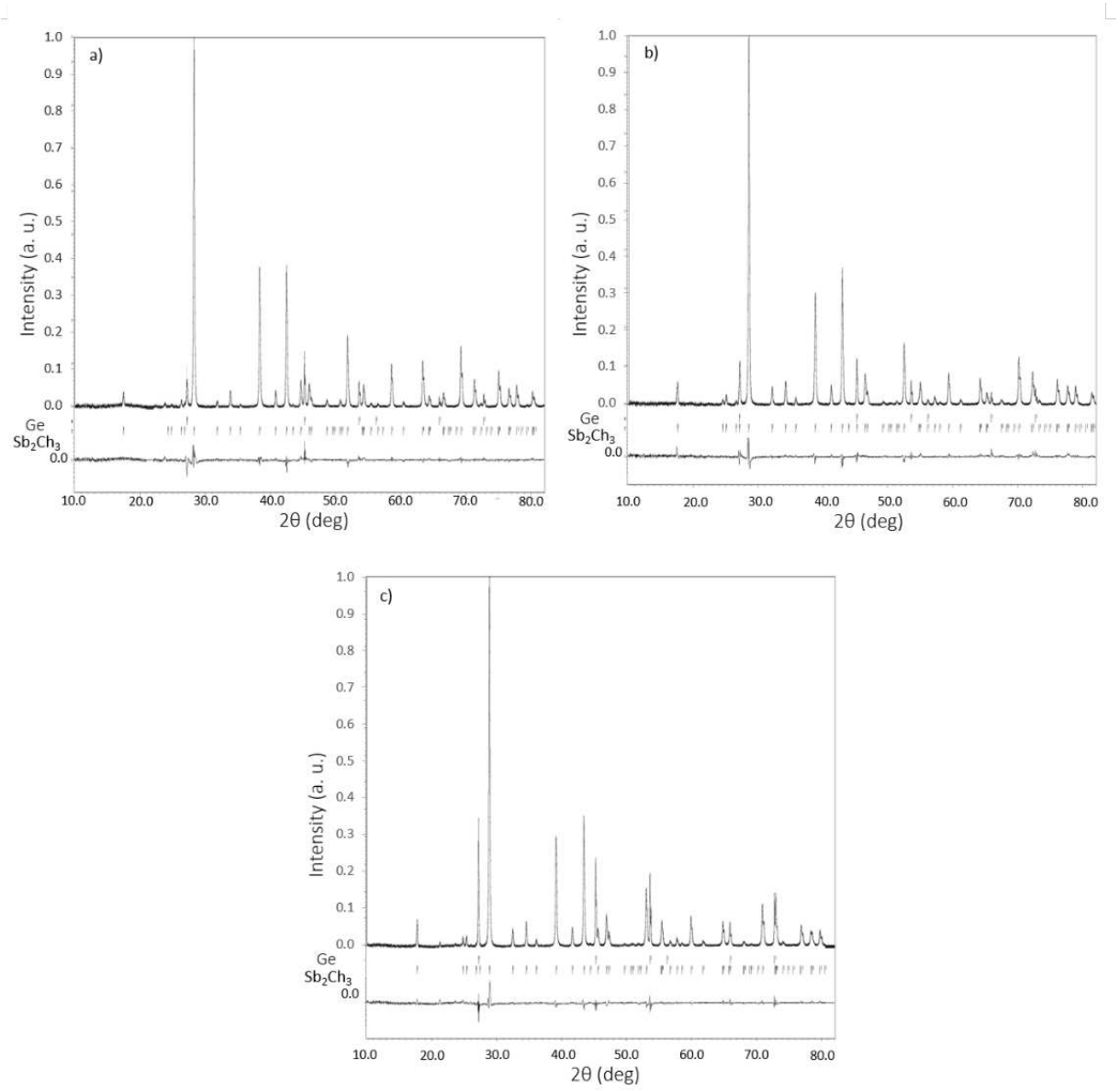

Fig. S3. The resulting Rietveld plots for the crystals of solid solutions $Sb_2(Te_{1-x}Se_x)_3$: (a) x≈0.1, (b) x≈0.3, (c) x≈0.5. The vertical markers show the positions calculated for the Bragg reflections (the second phase corresponds to monocrystalline Ge).

Section 4. The sensitivity of R-factor to lattice occupancy.

We have calculated the R-factor between all experimental patterns. They are presented in table S4. At the same time the Te 4d pattern varies for x<0.3, whereas the Se 3d pattern exhibits some changes for x=>0.3. This can be explained by the fact that the amount of Te atoms in the third atomic layer from the surface becomes negligible due to its preferential substitution by Se for x=>0.3. Electrons emitted from Te atoms in the first layer undergo predominantly forward scattering (i.e. in-plane scattering) and give minor contribution to the diffraction pattern, whereas the fifth layer yields weak intensity in the XPD patterns due to a short inelastic mean free path of electrons at a kinetic energy of 600 eV. For this reason, the Te 4*d* patterns is sensitive to Te atoms in the third atomic layer (Ch2 position). As they are missing for x=0.3 and 0.5 the diffraction patterns are similar (R=0.19). Contrary, for Se 3*d* patterns the difference increases upon

appearance of selenium atoms in the fifth and first atomic layers (Ch1 position). Therefore, such correlation in the behavior of Te and Se R-factors demonstrates that the R-factor is sensitive to the occupancy of lattice sites.

Table S4. The calculated R-factor between experimental patterns.

Pattern	$x_1 - x_2$		
	10-30	10-50	30-50
Sb 4d	0.1758	0.1773	0.2236
Te 4d	0.3029	0.3297	0.1960
Se 3d	0.0823	0.1446	0.1659
mean	0.1868	0.2283	0.2119

Section 5. Details of position occupancy calculations from the HAADF-STEM/EDX data

In addition to the study described in the main text, we also performed a more detailed EDX investigation to obtain a rough estimate of the chemical layer composition of the chemically different Te/Se layers. We followed a procedure similar to that described by Lu et al. [2,3], using the Sb-L (6.603 keV), Te-L (3.767 keV) and Se-K (11.210 keV) lines. First, we averaged the atomic resolution map (Fig. S4) to increase the signal-to-noise ratio. Next, we fitted the line profile of the elemental maps of the mixed positions with a combination of Gaussian functions using the Fityk software [4] (Fig. S4). The FWHM of the Gaussian peaks for each element was constrained to have the same value for different layers. Small differences can occur, because the FWHM depends on the beam spreading and channeling, which on its own depends on the chemical distribution within the column [3]. However, thin film conditions weaken the dependence. The fitted FWHM is 0.27 nm for Te-L and of 0.25 nm for Se-K.

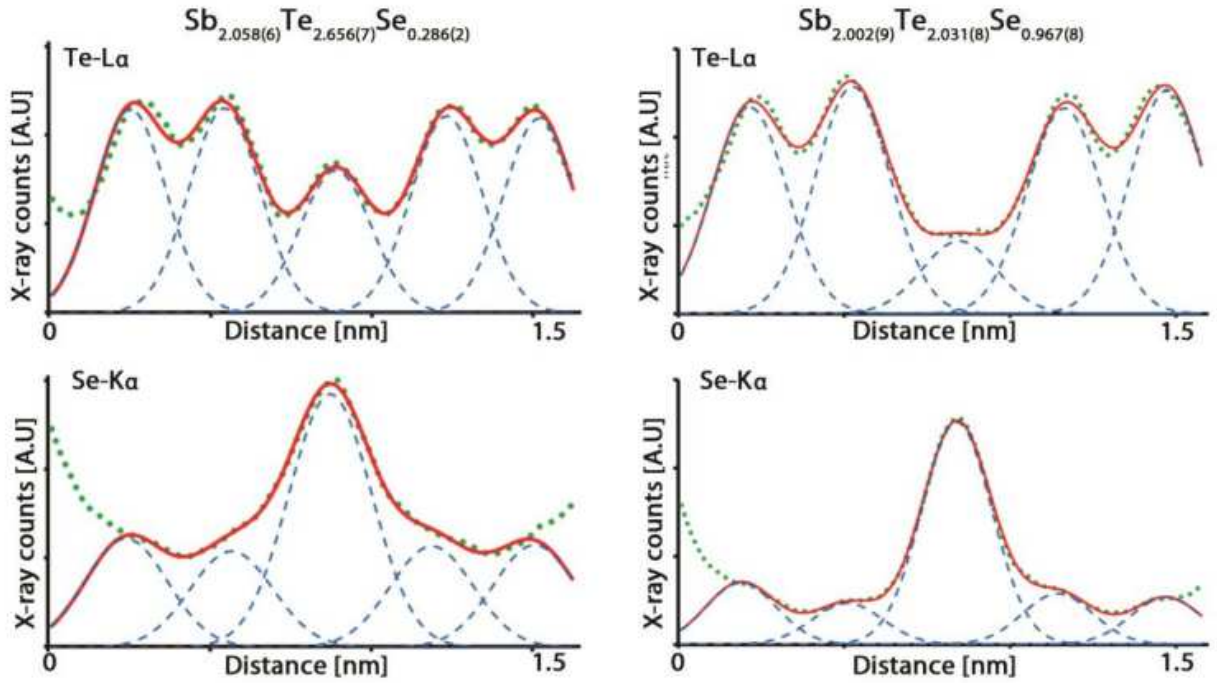

Fig. S4. The elemental Se and Te line profiles of the averaged HR-EDX maps in Fig. 4 (d) and (e): the experimental data (green) where Gaussian peaks are fitted at the different peak positions (blue) with the overall sum (red).

Then, we determine our own *k*-factors of the Cliff-Lorimer method [5] (assuming thin film conditions), which represent the scaling factor between the concentration ratio of two elements, C_{Te}/C_{Se}, and their corresponding characteristic X-ray intensity ratio I_{Te}/I_{Se}: $C_{Te}/C_{Se} = k_{Te,Se} \times I_{Te}/I_{Se}$. The counts ratio I_{Te}/I_{Se} is determined from the ratio of the sum of the areas under the Te and Se Gaussian peaks. The concentration ratio in atomic percent, C_{Te}/C_{Se}, was obtained from our STEM-EDX data. We can use the *k*-factors in the formulae $C_{Te}/C_{Se} = k_{Te,Se} \times I_{Te}/I_{Se}$ combined with $C_{Te} + C_{Se} = 1$ to determine the layer composition of the chemically different Te/Se layers. The error is calculated through error propagation with the k-factor variation $\Delta k/k \sim 0.1$ assuming that the error on the $Sb_2(Te_{1-x}Se_x)_3$ counts is equal to $\sqrt{I}$. The count variation ($\Delta I/I$) is thus negligible compared to the *k*-factor variation, when a reasonable amount of counts per element is available.

(1) Abajo, F. J. G. de; Hove, M. A. V.; Fadley, C. S. Multiple Scattering of Electrons in Solids and Molecules: A Cluster-Model Approach. *Phys Rev B* 2001, *63* (7), 075404. https://doi.org/10.1103/physrevb.63.075404.

(2) Lu, P.; Zhou, L.; Kramer, M. J.; Smith, D. J. Atomic-Scale Chemical Imaging and Quantification of Metallic Alloy Structures by Energy-Dispersive X-Ray Spectroscopy. *Sci Rep-uk* 2014, *4* (1), 3945. https://doi.org/10.1038/srep03945.

(3) Lu, P.; Xiong, J.; Benthem, M. V.; Jia, Q. Atomic-Scale Chemical Quantification of Oxide Interfaces Using Energy-Dispersive X-Ray Spectroscopy. *Appl Phys Lett* 2013, *102* (17), 173111. https://doi.org/10.1063/1.4804184.

(4) Wojdyr, M. Fityk : A General-Purpose Peak Fitting Program. *J Appl Crystallogr* 2010, *43* (5), 1126–1128. https://doi.org/10.1107/s0021889810030499.

(5) Williams, D. B.; Carter, C. B. Transmission Electron Microscopy, A Textbook for Materials Science. 2009. https://doi.org/10.1007/978-0-387-76501-3.